Karlsruhe Institute of Technology

Wave phenomena
analysis and numerics

High-resolution characterization of shallow aquifer by 2D viscoelastic full-waveform inversion of shallow seismic wavefield acquired at the Krauthausen test site

Lingli Gao, Yudi Pan, Andreas Rieder,
Thomas Bohlen, Weijian Mao

CRC Preprint 2022/27, June 2022

KARLSRUHE INSTITUTE OF TECHNOLOGY

CRC 1173

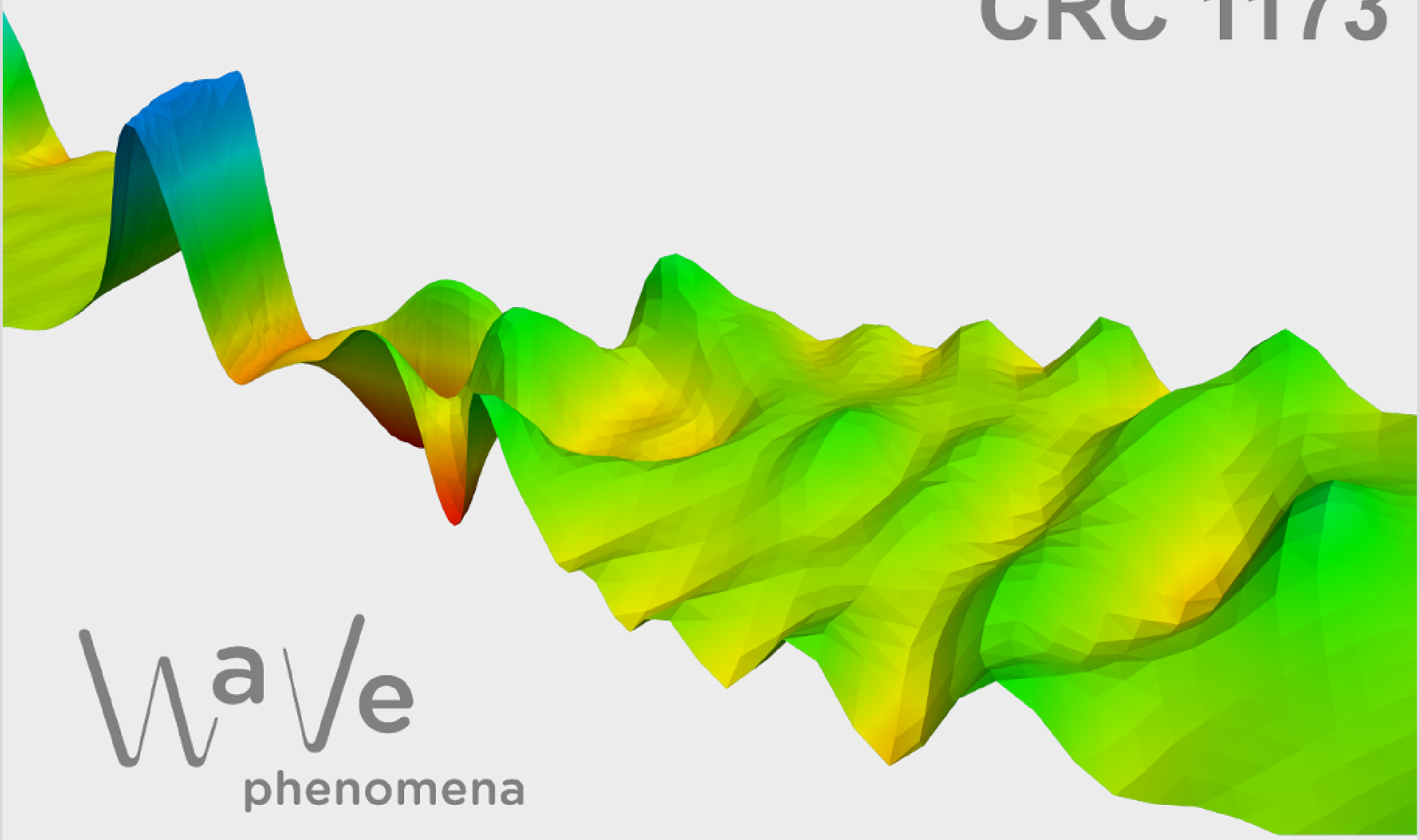

Wave phenomena

Participating universities

Universität Stuttgart

EBERHARD KARLS UNIVERSITÄT TÜBINGEN

TU WIEN

Funded by

DFG

ISSN 2365-662X

High-resolution characterization of shallow aquifer by 2D viscoelastic full-waveform inversion of shallow seismic wavefield acquired at the Krauthausen test site

Lingli Gao[a], Yudi Pan[b], Andreas Rieder[c], Thomas Bohlen[d], Weijian Mao[a]

[a] *Research Center for Computational and Exploration Geophysics, State Key Laboratory of Geodesy and Earth's Dynamics, Innovation Academy of Precision Measurement Technology and Science, Chinese Academy of Sciences, Wuhan* 430077*, China*
[b] *School of Geodesy and Geomatics, Wuhan University, Wuhan* 430079*, China*
[c] *Institute for Applied and Numerical Mathematics, Karlsruhe Institute of Technology (KIT), Karlsruhe* 76131*, Germany*
[d] *Geophysical Institute, Karlsruhe Institute of Technology (KIT), Karlsruhe* 76187*, Germany*

Abstract

Full-waveform inversion (FWI) method has been proved as an effective tool for high-resolution imaging of the subsurface. We have investigated the potential of shallow seismic-wave 2D viscoelastic FWI as a method in high-resolution hydrogeological near-surface characterization. FWI is applied to two orthogonal profiles acquired at the Krauthausen natural laboratory (Germany). The multiparameter models of viscoelastic FWI (P-and S-wave velocities, attenuation of P- and S-waves, density) show pronounced lateral variations below the profiles. The groundwater table is located at around 2 m, where a sudden P-wave velocity increase occurs. An S-wave low velocity layer exists at the depth of 4-6 m with a high Poisson's ratio value close to 0.5, which corresponds to a saturated sand layer know from previous studies.

A K-mean cluster analysis is used to correlate and integrate information contained in the inverted results. By considering the derived Poisson's ratio, P-wave, and S-wave velocities by FWI, we can convert the complex relationship between the multivariate data into a lithological meaningful zonation of the survey region. By comparing the lithological units in the alluvial aquifer with the cone penetration tests clusters, the face maps provide valuable information about the subsurface heterogeneity and connectivity. This experiment indicates that the multiparameter models derived by viscoelastic FWI contain usefull information for high resolution near-surface aquifer characterization.

Keywords: Aquifer characterization; Full-Waveform inversion; Rayleigh waves

1. Introduction

A reliable investigation of the aquifer is needed for environmental engineering tasks such as monitoring the groundwater flow and characterizing the contaminated transport. However, an accurate hydrogeological characterization is still challenging due to the typically heterogeneous unconsolidated gravel aquifer. Traditionally, a high vertical resolution of aquifer parameters can be obtained based on 1-D well data, e.g. core penetration test, tracer experiments. However, cost-efficiency and practical considerations lead to limited drilling numbers for 2D or even 3D geometry. Sedimentary deposits are usually composed of several distinct facies by recognizable boundaries at which the properties change (e.g. hydraulic parameters and/or velocities) (Gueting et al., 2015). Thus, non-invasive methods could help to characterize the geometry of the basement, classify the geophysical or/and hydrological units or facies in 2D and 3D versions. High-resolution

2-D or 3-D geophysical (mostly electromagnetic and electrical) methods have been increasingly used to investigate heterogeneous aquifer (Mouhri et al., 2013; Klotzsche et al., 2013; Gueting et al., 2015, 2017; Yu et al., 2021, 2022).

Seismic refraction methods have also been used to carry out hydrogeological investigations such as delineating groundwater aquifer in the subsurface (Jarvis and Knight, 2002; Bradford and John, 2002; Bradford and Sawyer, 2002; Murad et al., 2013). P-wave velocity (V_P) from seismic refraction methods can be used to determine the water table depth. Furthermore, seismic cross-well tomography (Moret et al., 2006; Becht et al., 2007) are performed for high-resolution aquifer characterization. However, P-wave velocities will be affected not only by fluid saturation, but also mineral composition, temperature, mineral texture, and other effects (Bauer et al., 2003). Due to the ambiguity of V_P values, joint studies of V_P and V_S can offer a suitable evaluation of aquifer characterization (Pasquet et al., 2015; Azhar et al., 2019). Besides, multichannel analysis of surface waves method (Xia et al., 1999) is included to verify S-wave velocities and interpretations from seismic refraction results (Konstantaki et al., 2013; Fabien-Ouellet and Fortier, 2014; Pasquet et al., 2015; Azhar et al., 2019).

In shallow seismic data, large velocity contrasts often generate wavefields with dominant higher modes of surface waves (Boaga et al., 2013; Gao et al., 2014, 2016). In this case, current surface-wave methods face uncertainty in the correct estimation and identification of multi-modal dispersion curves. Besides, the previous analysis of the ratio by the body waves commonly requires conducting two separate acquisitions for both V_P and V_S. As an alternative to conducting separate acquisition surveys, full waveform inversion (FWI) may cope with these limitations and can derive high-resolution multi-parameter models for complex geological structures simultaneously. With the rapid development of computational power, it has become increasingly popular to use 2D FWI of surface wave for reconstruction of near-surface models (Romdhane et al., 2011; Tran et al., 2013; Groos et al., 2014, 2017; Pan et al., 2016, 2019; Pan and Gao, 2020; Dokter et al., 2017). However, most of the previous studies invert for S-wave velocity only and neglect the effects of attenuation or simply implement a passive-viscoelastic FWI approach in which a fixed prior estimation of the attenuation model is used in the forward modeling to compensate for viscoelastic effects. When facing strong spatial variation of strong attenuation in shallow subsurface where a high level of heterogeneity exists, simply neglecting the viscoelastic effect might deteriorate the reconstruction of S-wave velocity (Groos et al., 2014; Gao et al., 2020). Multi-parameter full waveform inversion could reconstruct both velocity and attenuation simultaneously (Métivier et al., 2013; Yang et al., 2018; Fabien-Ouellet et al., 2017; Athanasopoulos et al., 2020; Gao et al., 2021). Besides, 3D FWI of the near-surface parameter reconstruction is also becoming feasible in the recent years (Irnaka et al., 2019; Mirzanejad and Tran, 2019; Pan et al., 2021).

In this paper, we present a case study for aquifer characterization with 2D viscoelastic FWI. We conducted a field experiment at the Krauthausen test site in Northwest Germany, where seismic data were acquired along two orthogonal lines. Intensive cone penetration tests (CPT) have been conducted there, together with an intensive investigation of Ground Penetrating Radar (GPR) data. Due to the extensive set of subsurface information retrieved, this test site offers an excellent opportunity to test the potential of seismic data for aquifer characterization. The detailed subsurface geological information about the test site is provided in Section 2. Firstly, the seismic FWI is applied to estimate both P- and S-wave velocity, attenuation of P and S waves, and thereby Poisson's ratio. The description of the methodology is presented in Section 3. In Section 4, the outcome of the inversion enables us to understand in detail the lateral variation in layer thickness and properties. Later, a cross-sectional map showing the spatial distribution of the subsurface presents the connectivity of the obtained two profiles. Secondly, a K-mean cluster analysis is conducted for the facies classification by considering their V_p, V_s, and Poisson's ratio. The clustering result shows the spatial distribution of different facies in the aquifer. Finally, we discuss the reliability of the facies classification by comparing the distribution of facies obtained from seismic FWI to the cluster analysis results of the data from CPT.

2. Field data application

2.1. Description of the test site

The goal of seismic survey was to characterize the hydrological situation at the Krauthausen test site. It is located in northwest Germany between cities of Jülich and Düren and was set up in 1993 by research center Jülich. Over the last decades, the Krauthausen site has been intensively investigated with the goal of studying the spatial distribution of aquifer with a broad spectrum of methods, including tracer experiments (Vereecken et al., 2000), cone penetration tests (Tillmann et al., 2008), and geophysical imaging methods (Klotzsche et al., 2013; Gueting et al., 2015, 2017). The present studies showed that the uppermost aquifer is approximately 10 m thick and composed of alluvial terrace sediments (Fig. 1). The top of the aquifer was divided into three layers: a poorly-sorted gravel layer extending from 1-4 m depth; a well-sorted sand layer extending from 4-6 m depth; and a bottom layer composed of sandy to gravel grain size, which extends from 6-11.5 m depth. The groundwater level shows variations from 1 to 3 m depth depending on the annual season. It is worth to note the generalized aquifer shown in Fig.1 represents a conceptual model of the geologic sequence for the aquifer, which is an oversimplification of the aquifer's true structure.

Most recently GPR full-waveform inversion revealed the heterogeneous nature of the uppermost aquifer with higher spatial resolution and yielded a tomographic image with a significantly improved level of details (Klotzsche et al., 2013; Gueting et al., 2015, 2017). Besides, CPT were performed in the centre of the test site with a vertical sampling interval for all measurement set as 10 cm. At each CPT location, vertical profiles are down to an average depth of approximately to 13 m (Gueting et al., 2015), which could across the entire thickness of the uppermost aquifer.

2.2. Data acquisition

With the aim of delineating the lateral variation of the subsurface in the Krauthausen test site, the seismic surveys were conducted along two perpendicular lines. The acquisition was implemented on the 29th and 30th of September 2018 under rela-

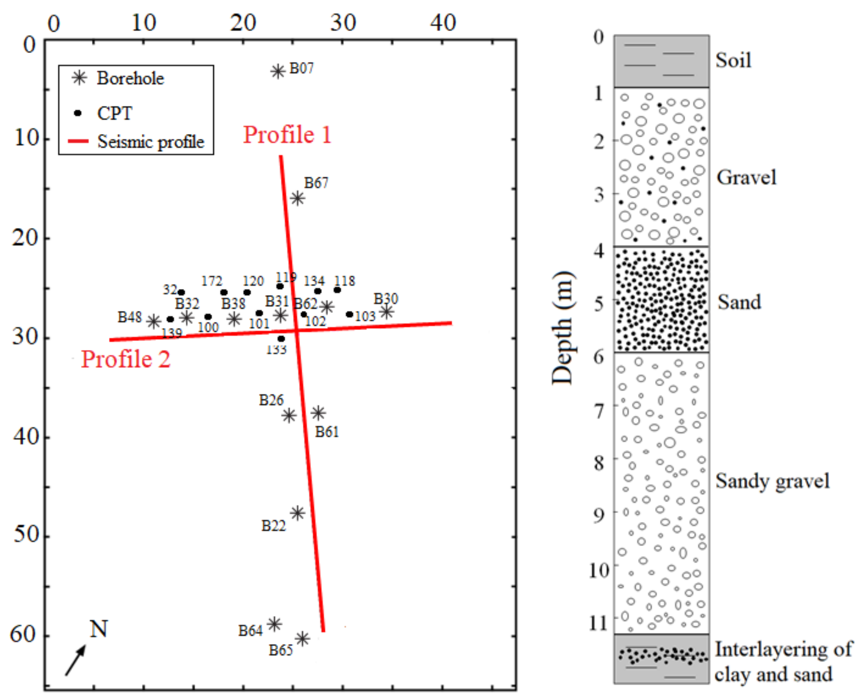

Figure 1: Left: Schematic diagram map of the Krauthausen test site including the two seismic profiles and adjacent boreholes and CPT positions. The asterisk and the dark dots represent the location of boreholes and the cone penetration tests, respectively. Right: A conceptual geologic cross-section of the uppermost aquifer in Krauthausen test site according to Döring (1997) and Tillmann et al. (2008).

tively dry soil conditions (Athanasopoulos, 2021). Two survey lines (P1 and P2) were set in the central part of the test site, where closely spaced boreholes and CPTs were available. The acquisition geometry of P1 consisted of 14 shots as vertical-force sources with a spacing of 4 m and 48 receivers with a spacing of 1 m. The acquisition geometry of P2 consisted of 11 shots generated by vertical-force sources with a spacing of 4 m and 36 receivers with a spacing of 1 m. The sources were generated by hammer blows hitting a steel plate. P1 crossed the boreholes 67, 31/62, 26/61,22, 64, and 65, with the last one being the end of the receiver line (Athanasopoulos, 2021). P2 was placed near the boreholes 48, 32, 38, 31, 62, and 30. A detailed map of the Krauthausen test site with two profiles is shown in Fig. 1.

3. Methodology

FWI, as a data-fitting iterative procedure, aims to minimize the differences between the simulated data and the measured data here defined as,

$$J(\boldsymbol{m}) = \frac{1}{2}\sum_{s=1}^{N_s}\sum_{r=1}^{N_r} \|\boldsymbol{d}_{cal}(\boldsymbol{m})(\boldsymbol{x}_r, t; \boldsymbol{x}_s) - \boldsymbol{d}_{obs}(\boldsymbol{x}_r, t; \boldsymbol{x}_s)\|^2. \quad (1)$$

Here, the model properties (such as velocity, attenuation, density) of the subsurface are denoted by the vector $\boldsymbol{m}$. Further, $\boldsymbol{d}_{obs}$ and $\boldsymbol{d}_{cal}$ represent the observed and synthetic seismograms computed in the model $\boldsymbol{m}$, associated with the source $\boldsymbol{x}_s$ and receiver $\boldsymbol{x}_r$, respectively. N_s and N_r represent the source and receiver numbers, respectively. And t is the time.

The inversion is formulated as the minimization of the misfit function J. To the large size of the model space, the global optimization method is computationally expensive for solving problems Xing and Mazzotti (2019). Hence, FWI is usually performed through the iterative local optimization technique based on gradients which can be calculated efficiently by the adjoint state method. In the framework of local non-linear optimization methods, an iterative sequence $\boldsymbol{m}_{k+1}$ is built by starting from an initial guess $\boldsymbol{m}_0$ with a descent direction $\Delta\boldsymbol{m}_k$:

$$\boldsymbol{m}_{k+1} = \boldsymbol{m}_k + \lambda\Delta\boldsymbol{m}_k \tag{2}$$

where k is the iteration number, and λ is the step length at iteration k estimated through a line search process with parabolic fitting (Nocedal and Wright, 2006). The model perturbation, $\Delta\boldsymbol{m}_k$, can be given by gradient-based (e.g. steepest descent, conjugate gradient) and Newton-based method (e.g. truncated Newton method, Gauss-Newton method).

Multi-parameter FWI is challenging due to the potentially strong interparameter crosstalks (Virieux and Operto, 2009; Operto et al., 2013). Updating the model perturbation with gradient only cannot decipher between different parameters. Researches show that Newton-based methods generate less crosstalk and artefacts in the reconstructed models (Métivier et al., 2013; Yang et al., 2018; Gao et al., 2021). In this case, we implement the multi-parameter viscoelastic FWI with the matrix-free Gauss-Newton algorithm. The general scheme for solving the multi-parameter includes two loops: an external loop for Gauss-Newton update and the inner loop is the linear conjugate gradient method. For a more detailed description of the inversion procedure and its implementation, the reader could refer to Bohlen et al. (2021) and Chen and Sacchi (2020).

An important requirement for the full-waveform inversion is adequate starting models (Pan et al., 2019). To derive adequate V_S starting models, we conducted the Multi-channel analysis of Surface wave (MASW) method for profile P1 (Xia et al. (1999)). The initial 1D V_P model is calculated from the first-arrival times of the refracted waves. The initial ρ models are obtained through Gardner's relationship. For the initial Q_P, $Q_P = 2 * Q_S$ is assumed. Linear gradient models are used as the initial models for inversion. All five initial models are shown in the first column of Fig. 2. Before the inversion, a 3D to 2D transformation (Forbriger et al., 2014) must be applied to the field data. Schäfer et al. (2014) proved the applicability of this 3D to 2D transformation even to models with smooth lateral heterogeneities. To reduce the non-linearity of the inverse problem and avoid the inversion being trapped into a local minimum, a sequential FWI workflow of low-pass and band-pass filtered data with different bandwidth is applied (Bunks et al., 1995). In our example the multi-stage inversion strategy with the frequency band starts with low-pass filter data with 0 - 15 Hz. The frequency content is progressively increased by 5 Hz until 40 Hz is reached, and a highest frequency band of 60 Hz is used in the last stage.

4. Results

In this section, we present the inverted model obtained from multiparameter viscoelastic FWI. A minimum of three iterations is guaranteed in each stage, and the inversion moved to the next stage when the relative decrease in the misfit value is less than 1%. We estimate a source time function correction filter by a stabilized deconvolution (Groos et al., 2014) and use it to update the source time function at the beginning of each frequency stage.

The multi-parameter inversion results along both profiles are shown in Fig. 2. The reconstructed V_S structure shows a high level of heterogeneity. Below the P1 profile, V_S is low within the upper 2 m where the loamy soil layer has developed (Döring, 1997; Gueting et al., 2015). Referring to the prior geological model (Fig. 1) of the test site (Tillmann et al., 2008), there is a poorly sorted gravel layer that exists in the depth of about 2 - 4 m, where the V_S increases. A layer of low V_S shows up at the depths of 4 - 6 m, which correlates well with previous studies that a sandy layer exists. Especially, the P2 profile shows a more continuous and distinct boundary of this sand layer, which can also be comfirmed in Athanasopoulos (2021). Below this layer, V_S increases, which agrees to the borehole information that the soil content change from sand to gravel. Overall, the S-velocity model is distinguished by sub-horizontal structures, which is consistent with stratigraphic layering in the gravel and sand deposits at the Krauthausen test site.

For V_P results from both P1 and P2 profiles, both of them did not show strong horizontal heterogeneity compared to V_S results. This low resolution can be at-

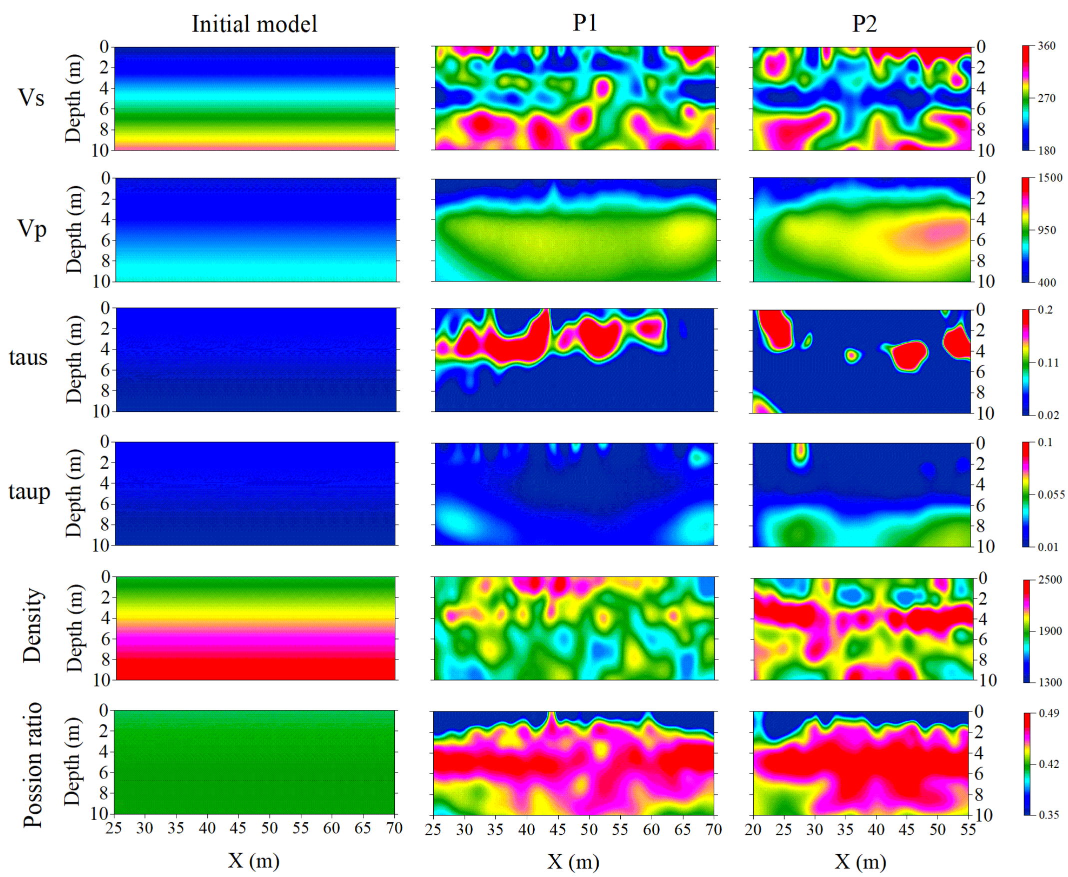

Figure 2: Final models below both profiles obtained by 2D viscoelastic FWI. The initial models are represented in the first column. The second column and third column represent the reconstruction results of profiles 1 and 2, respectively. Since we only use one relaxation mechanism (Bohlen, 2002; Gao et al., 2021), τ_s and τ_p are approximated as $2/Q_s$ and $2/Q_p$ where Q_s and Q_p are the quality factor of S and P wave, respectively.

tributed to the large wavelength of the P-wave at low frequencies. Nevertheless, consistent structures in the V_P results can be observed. We can see the P-wave velocity is suddenly increased at the depth of about 2 m, where the groundwater table exists. It is confirmed that the effect of water saturation on V_P is significant. This sudden increase could thus be an indicator of groundwater table level in the near-surface cases (Pasquet et al., 2015).

The inverted attenuation models of both profiles are given in Fig. 2. We inverted for the so-called tau parameter which relates to the quality factors of P- and S-waves by $Q_s \approx 2/\tau_s$ and $Q_p \approx 2/\tau_p$. For the τ_s results, we can observe clear strong attenuation anomalies located at the depth of 4-6 m. For the τ_p results, as can be seen that the results are significantly contaminated by some artefacts. This could be interpreted as attenuation is the weakest parameter and can be easily affected by velocity and density errors (Fabien-Ouellet et al., 2017; Gao et al., 2020, 2021). As to the inverted density model (Fig. 2) in P1, the reconstructed results did not provide reliable information about the surface layers. With regards to the density model in P2, it delineates a high-density layer at about 3-5 m. Due to the low sensitivity of the Rayleigh wave to density, the reliability of the density results needed to be the verified by some secondary data.

4.1. Poisson's ratio

Experimental developments (Bachrach et al., 2000; Foti et al., 2002; Uyanik, 2011) showed that the saturation could affect the P- and S-wave velocities (V_p and V_s). This gives a hint that the joint studies of V_P and V_S, especially by estimating

Poisson's ratio could provide a suitable evaluation of the saturation of aquifer characterization (Bachrach et al., 2000; Konstantaki et al., 2013; Pasquet et al., 2015).

Using the inverted V_P and V_S, we also calculate the Poisson's ratio as

$$\nu = \frac{V_P^2 - 2V_S^2}{2(V_P^2 - V_S^2)}. \tag{3}$$

The computed ν results obtained by V_P and V_S in Fig.2 are remarkably similar (Fig. 3f). As can be seen in the initial Poisson's ratio model, the initial value of Poisson's value is 0.42. While the Poisson's ratio values of the reconstructed results for both profiles range from 0.3 to 0.5 (second and third column in Fig. 2), which are typical of unsaturated and saturated media, respectively (Pasquet et al., 2015, 2016). Lower Poisson's ratio values at the shallow subsurface may be explained by the dry soil condition on the top layer (Athanasopoulos, 2021). Specifically, the Poisson's ratio closes to 0.5 at the depth of 4-6 m, might indicate a highly saturated layer located there, and corresponds to existed sandy layer. This result also shows a good agreement in both profiles together with the previous study (Döring, 1997; Gueting et al., 2015).

We show the results of all inverted parameters from both profiles into a 3D layout (Fig. 3). The cross-sections show a good agreement in the majority of the results. The low S-wave velocity layer with a high Poisson's ratio delineates the high saturated sandy layer at the depth of 4-6 m. The sudden increase in V_P indicates the location of the water level. To further evaluate the inverted results,

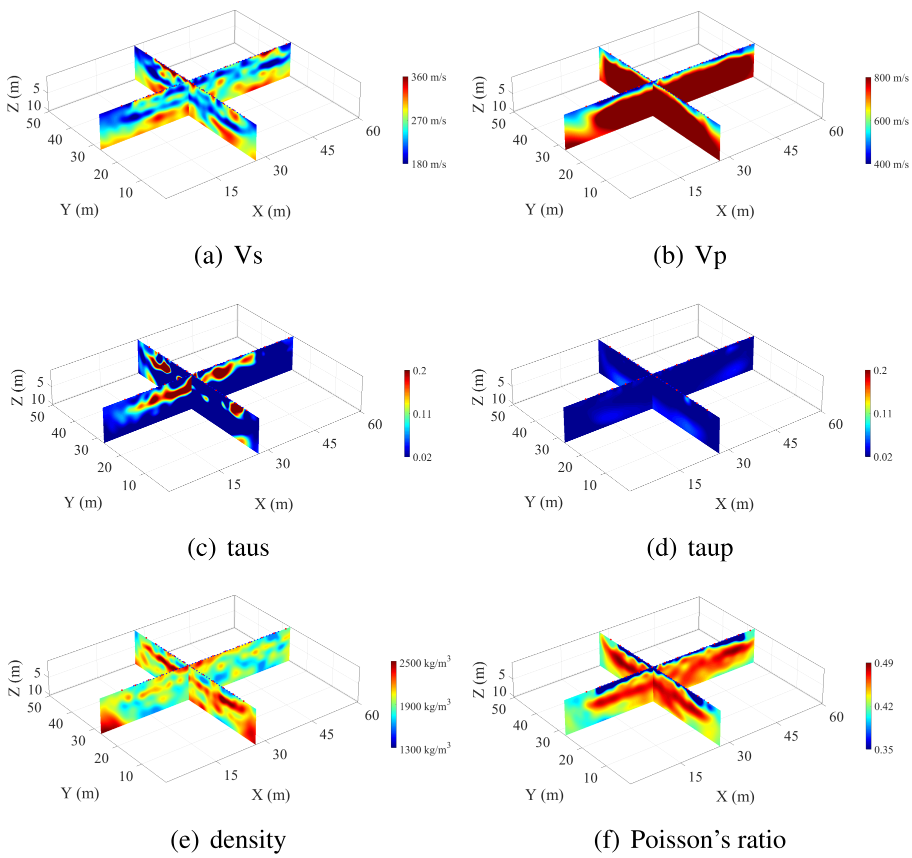

(a) Vs (b) Vp

(c) taus (d) taup

(e) density (f) Poisson's ratio

Figure 3: Cross-section of the reconstructed models of both profiles by multi-parameter FWI. (a) V_S; (b) V_P; (c) τ_s; (d) τ_p; (e) ρ; (f) Poisson's ratio. The red dots and blue triangles represent the shots and receivers, respectively.

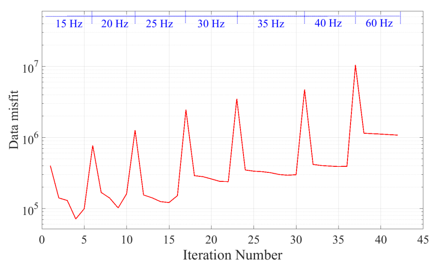

(a) Data misfit of profile 1

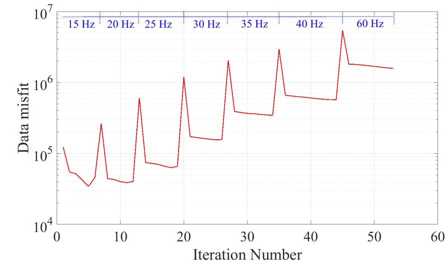

(b) Data misfit of profile 2

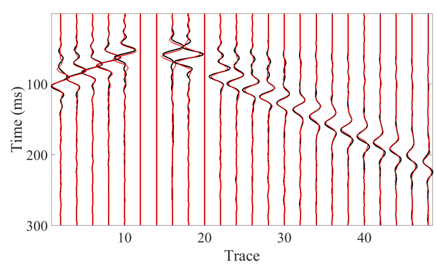

(c) Shot 5 in profile 1

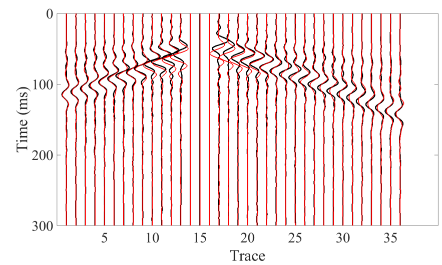

(d) Shot 5 in profile 2

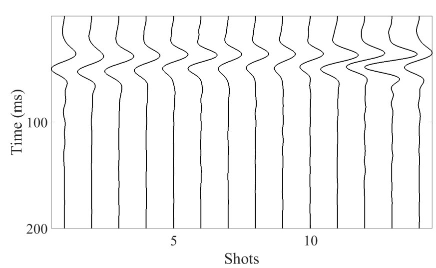

(e) Estimated STF of profile 1

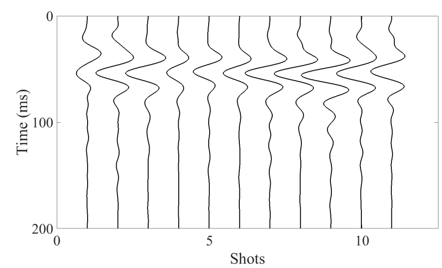

(f) Estimated STF of profile 2

Figure 4: (a) and (b) represent data misfit for P1 and P2, respectively; Jumps of increasing misfit value correspond to changes of the FWI workflow stage. (c) and (d) represent the comparison of the trace-normalized observed (black) and synthetic seismograms (red) for shot 5 in P1 and P2, respectively. The shot gather for the shot 5 in profiles 1 is displayed with every two traces. (e) and (f) represent the estimated source time functions of data acquire along P1 and P2, respectively.

the final data misfits are shown in Figs. 4a and b. We note that the data misfit reduces. We also compare the final synthetic seismogram with the observed data in Fig. 4e and f. In both profiles, the synthetic seismogram fits the observed data in satisfactory, which indicates a successful explanation of the observed wavefield by the final multi-parameter models. The final estimated source-time functions (STF) for every shot in both profiles are shown in Fig. 4e and f. In both cases, we can observe similar wavelets for all source locations, indicating that estimated source time functions used for the inversion are fairly reliable.

4.2. Cluster analysis

Cluster analysis, as a multivariate statistical method, can be used to correlate and integrate information of a broad range of observations into relatively homogeneous units by dividing the data based on their distances in the multi-dimensional parameter spaces instead of a prior information about the classification. K-means algorithm (Macqueen, 1967) has been proven as a useful approach to extract the basic structural information from various types of multivariate geophysical data (Tronicke et al., 2004; Dietrich and Tronicke, 2009). Shallow-seismic wavefields are dominated by Rayleigh wave, which has a high sensitivity to S-wave velocity. Meanwhile, P-wave velocity and Poisson's ratio are sensitive to the saturation situation. We applied the K-mean cluster analysis algorithm in three data spaces (V_P, V_S, ν). As data pre-processings, we normalized the velocity and Poisson's ratio to assign similar weights before the analysis. Specification of the number of clusters is a critical step in the cluster analysis. Generally, the number of clusters can be assigned according to the variance ration criterion (VRC) (Calinski and Harabasz, 1974). Here, according to previous partitions for the GPR inversion results and CPT results, we manually set a cluster number of three in this case (Gueting et al., 2015).

The results of the cluster analysis are shown in Fig. 5. Although the velocity and Poisson's ratio results in Fig. 2 both have an overall layered character, however, the correlation between most structures is not clear. On the basis of the corresponding cluster analysis considers with three data spaces, the spatial distribution of these homogeneous units is shown in Fig. 5. Cluster 1 is characterized by higher P-wave velocity, higher Poisson's ratio, but with a lower S-wave velocity. Cluster 2 is characterized by lower P-wave velocity, lower Poisson's ratio, but with a higher S-wave velocity. Cluster 3 is characterized by an intermediate velocity and Poisson's ratio. Although the characterization of the subsurface has been reduced to only three-parameter groups, the clustered section delineates the major structural feature of the original models.

In order to validate our results of cluster analysis of seismic data, we compare the seismic data clusters with the cluster analysis results of CPT data (Gueting et al., 2015) in Fig. 5. The spatial distribution of the clusters shows a nice agreement, especially for the depth of 4-6 m. From the description of the grain size distribution in borehole B32 by Gueting et al. (2015), the CPT cluster 1 corresponds to in those depths where the grain size analysis shows gravel; CPT cluster 2 corresponds to in those depths where the grain size analysis shows sand, and CPT cluster 3 corresponds to in those depths where the grain size analysis shows an

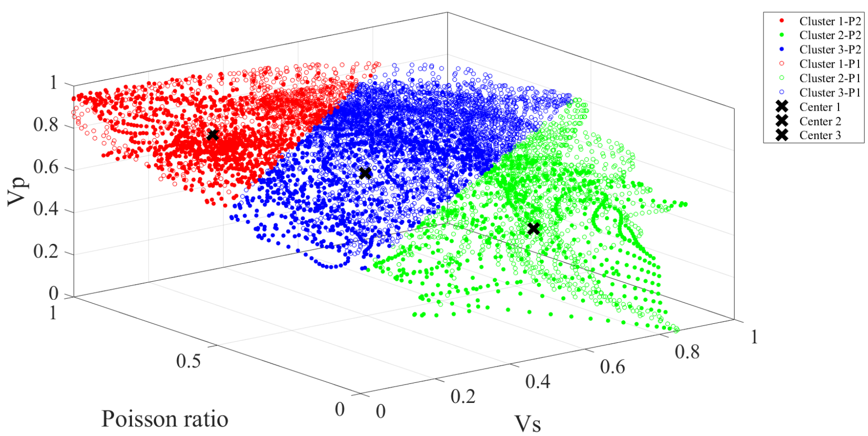

(a) Cluster analysis

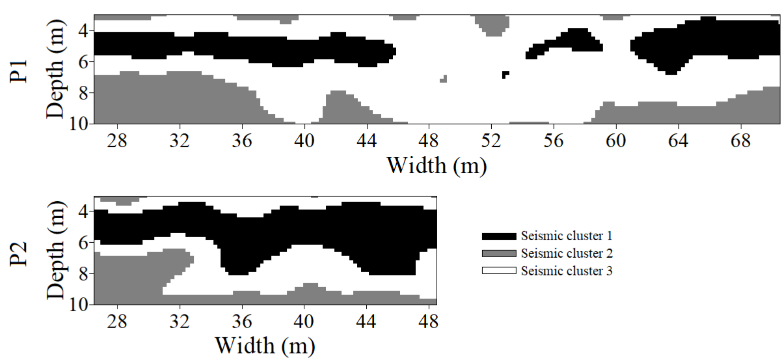

(b) Cluster sections of two profile P1 (upper) and P2 (lower)

Figure 5: Cluster analysis. (a) The 3D plot of P-wave velocity, S-wave velocity, and Poisson's ratio. The red, blue and green dots are divided by the K-mean cluster analysis. The crosses delineate three cluster centres. (b) Cluster sections of the two profiles P1 and P2 according to the classification in (a). Numbers and colours refer to specific clusters.

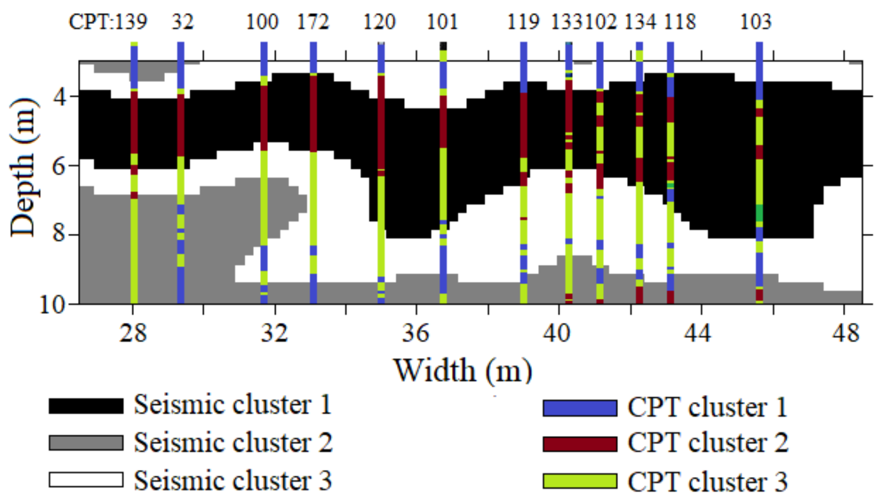

Figure 6: Cluster comparison between the seismic results and CPT results. Cluster profile P2 according to the classify in Fig. 5(a). CPT clusters are referred to Gueting et al. (2015).

intermediate material such as gravelly sand or as sandy gravel. The water content histograms, which is related to porosity also show that a relatively high porosity for CPT cluster 2, relatively small porosity for CPT cluster 1, and an intermediate porosity for CPT cluster 3, which are corresponded to the relative velocity and Poisson's ratio's changes in seismic clusters.

5. Conclusions

FWI of shallow seismic P- and Rayleigh waves proved to be a powerful tool for the reconstruction of viscoelastic multiparameter models of the shallow subsurface. Typically, the solution of the inverse problem is non-unique and, thus, there may be various solutions that differ in details but show equivalent overall fits to the data. We have explored the potential of applying the FWI method in a well-studied alluvial aquifer test site, which can offer secondary information to evaluate the reliability of the obtained inverted results. In addition, the benefit of the parameters attenuation and mass density with information potential would be studied in the future.

Cluster analysis of the multivariate seismic inversion results defined three different facies in the aquifer cross-section. The classification of facies was confirmed by the previous cluster analysis of CPT data. Moreover, the spatial distribution of facies in seismic data showed a nice agreement with the spatial distribution of CPT clusters. Comparison of the facies distribution with the previous analysis showed that the derived lithological units correlate with the changes in grain size and porosity. Overall, the experiment indicates that FWI of seismic data can produce high-resolution results of the subsurface. Combined with cluster analysis of the multivariate inverted data, FWI could give us an applicable approach to classify geophysical facies. Integrating other geophysical and geotechnical parameters (e.g. GPR data, grain size, and flowmeter data) can help to better characterize the aquifer.

6. Acknowledgements

The authors thank for Martin Pontius, Niko Athanasopoulos and other students attending the Geoverbund ABC-J 2018 Summer School on Hydrogeophysics at Forschungszentrum Jülich for their generous help in data acquisitions. This work was funded by the National Science Foundation of China under Grant 42130808 and the Deutsche Forschungsgemeinschaft (DFG, German Research Foundation), Project ID 258734477-SFB 1173.

References

Athanasopoulos, N., 2021. Challenges in near-surface seismic full-waveform inversion of field data. Ph.D. thesis. Karlsruher Institut für Technologie (KIT).

Athanasopoulos, N., Manukyan, E., Bohlen, T., Maurer, H., 2020. Time–frequency windowing in multiparameter elastic FWI of shallow seismic wavefield. Geophysical Journal International 222, 1164–1177.

Azhar, A.S.b., Latiff, A.H.A., Lim, L.H., Gödeke, S.H., 2019. Groundwater investigation of a coastal aquifer in brunei darussalam using seismic refraction. Environmental Earth Sciences 78, 1–17.

Bachrach, R., Dvorkin, J., Nur, A.M., 2000. Seismic velocities and poisson's ratio of shallow unconsolidated sands. Geophysics 65, 559–564.

Bauer, K., Schulze, A., Ryberg, T., Sobolev, S.V., Weber, M., 2003. Classification of lithology from seismic tomography: a case study from the messum igneous complex, namibia. Journal of Geophysical Research: Solid Earth 108.

Becht, A., Bürger, C., Kostic, B., Appel, E., Dietrich, P., 2007. High-resolution aquifer characterization using seismic cross-hole tomography: An evaluation experiment in a gravel delta. Journal of hydrology 336, 171–185.

Boaga, J., Cassiani, G., Strobbia, C.L., Vignoli, G., 2013. Mode misidentification in Rayleigh waves: Ellipticity as a cause and a cure. Geophysics 78, EN17–EN28.

Bohlen, T., 2002. Parallel 3-D viscoelastic finite difference seismic modelling. Computers & Geosciences 28, 887–899.

Bohlen, T., Fernandez, M.R., Ernesti, J., Rheinbay, C., Rieder, A., Wieners, C., 2021. Visco-acoustic full waveform inversion: From a DG forward solver to a Newton-CG inverse solver. Comput. Math. Appl. 100, 126–140.

Bradford, J.H., John, H., 2002. Depth characterization of shallow aquifers with seismic reflection, part i—the failure of nmo velocity analysis and quantitative error prediction. Geophysics 67, 89–97.

Bradford, J.H., Sawyer, D.S., 2002. Depth characterization of shallow aquifers with seismic reflection, part ii—prestack depth migration and field examples. Geophysics 67, 98–109.

Bunks, C., Saleck, F.M., Zaleski, S., Chavent, G., 1995. Multiscale seismic waveform inversion. Geophysics 60, 1457–1473.

Calinski, T., Harabasz, J., 1974. A dendrite method for cluster analysis: Communications in statistics. Communications in Statistics 3, 1–27.

Chen, K., Sacchi, M.D., 2020. Time-domain elastic Gauss–Newton full-waveform inversion: a matrix-free approach. Geophysical Journal International 223, 1007–1039.

Dietrich, P., Tronicke, J., 2009. Integrated analysis and interpretation of cross-hole p- and s-wave tomograms: a case study. Near Surface Geophysics 7, 101–109.

Dokter, E., KöHn, D., Wilken, D., De Nil, D., Rabbel, W., 2017. Full waveform inversion of SH- and Love-wave data in near-surface prospecting. Geophysical Prospecting 65, 216–236.

Döring, U., 1997. Transport der reaktiven Stoffe Eosin, Uranin und Lithium in einem heterogenen Grundwasserleiter. Ph.D. thesis. Christian Albrecht Universität Kiel.

Fabien-Ouellet, G., Fortier, R., 2014. Using all seismic arrivals in shallow seismic investigations. Journal of Applied Geophysics 103, 31–42.

Fabien-Ouellet, G., Gloaguen, E., Giroux, B., 2017. Time domain viscoelastic full waveform inversion. Geophysical Journal International 209, 1718–1734.

Forbriger, T., Groos, L., Schafer, M., 2014. Line-source simulation for shallow-seismic data. part 1: theoretical background. Geophysical Journal International , 1387–1404.

Foti, S., Lai, C.G., Lancellotta, R., 2002. Porosity of fluid-saturated porous media from measured seismic wave velocities. Géotechnique 52, 359–373.

Gao, L., Pan, Y., Bohlen, T., 2020. 2-d multiparameter viscoelastic shallow-seismic full-waveform inversion: reconstruction tests and first field-data application. Geophysical Journal International 222, 560–571.

Gao, L., Pan, Y., Rieder, A., Bohlen, T., 2021. Multiparameter viscoelastic full-waveform inversion of shallow-seismic surface waves with a pre-conditioned truncated Newton method. Geophysical Journal International , 3.

Gao, L., Xia, J., Pan, Y., 2014. Misidentification caused by leaky surface wave in high-frequency surface wave method. Geophysical Journal International 199, 1452–1462.

Gao, L., Xia, J., Pan, Y., Xu, Y., 2016. Reason and condition for mode kissing in MASW method. Pure and Applied Geophysics 173, 1627–1638.

Groos, L., Schäfer, M., Forbriger, T., Bohlen, T., 2014. The role of attenuation in 2D full-waveform inversion of shallow-seismic body and Rayleigh waves. Geophysics 79, R247–R261.

Groos, L., Schäfer, M., Forbriger, T., Bohlen, T., 2017. Application of a complete workflow for 2D elastic full-waveform inversion to recorded shallow-seismic Rayleigh waves. Geophysics 82, R109–R117.

Gueting, N., Klotzsche, A., van der Kruk, J., Vanderborght, J., Vereecken, H., Englert, A., 2015. Imaging and characterization of facies heterogeneity in an alluvial aquifer using gpr full-waveform inversion and cone penetration tests. Journal of hydrology 524, 680–695.

Gueting, N., Vienken, T., Klotzsche, A., van der Kruk, J., Vanderborght, J., Caers, J., Vereecken, H., Englert, A., 2017. High resolution aquifer characterization using crosshole gpr full-waveform tomography: Comparison with direct-push and tracer test data. Water Resources Research 53, 49–72.

Irnaka, T.M., Brossier, R., Métivier, L., Bohlen, T., Pan, Y., 2019. Towards 3d

9c elastic full waveform inversion of shallow seismic wavefields - case study Ettlingen line, in: EAGE 2019 Annual Meeting.

Jarvis, K.D., Knight, R.J., 2002. Aquifer heterogeneity from sh-wave seismic impedance inversion. Geophysics 67, 1548.

Klotzsche, A., van der Kruk, J., Linde, N., Doetsch, J., Vereecken, H., 2013. 3-d characterization of high-permeability zones in a gravel aquifer using 2-d crosshole gpr full-waveform inversion and waveguide detection. Geophysical Journal International 195, 932–944.

Konstantaki, L.A., Carpentier, S., Garofalo, F., Bergamo, P., Socco, L.V., 2013. Determining hydrological and soil mechanical parameters from multichannel surface-wave analysis across the alpine fault at inchbonnie, new zealand. Near Surface Geophysics 11, 435–448.

Macqueen, J.B., 1967. Some methods for classification and analysis of multivariate observations, in: Proceedings of the Fifth Berkeley Symposium on Mathematical Statistics and Probability.

Métivier, L., Brossier, R., Virieux, J., Operto, S., 2013. Full waveform inversion and the truncated Newton method. SIAM Journal on Scientific Computing 35, B401–B437.

Mirzanejad, M., Tran, K.T., 2019. 3d viscoelastic full waveform inversion of seismic waves for geotechnical site investigation. Soil Dynamics and Earthquake Engineering 122, 67–78.

Moret, G.J., Knoll, M., Barrash, W., Clement, W.P., 2006. Investigating the stratigraphy of an alluvial aquifer using crosswell seismic traveltime tomography. Geophysics 71, B63–b73.

Mouhri, A., Flipo, N., Rejiba, F., de Fouquet, C., Bodet, L., Kurtulus, B., Tallec, G., Durand, V., Jost, A., Ansart, P., Goblet, P., 2013. Designing a multi-scale sampling system of stream-aquifer interfaces in a sedimentary basin. Journal of Hydrology 504, 194–206.

Murad, A., Baker, H., Mahmoud, S., Gabr, A., 2013. Detecting groundwater levels using the shallow seismic method: Case study. Journal of Hydrologic Engineering 19, 867–876.

Nocedal, J., Wright, S.J., 2006. Numerical optimization. Springer .

Operto, S., Gholami, Y., Prieux, V., Ribodetti, A., Brossier, R., Metivier, L., Virieux, J., 2013. A guided tour of multi-parameter full waveform inversion with multi-component data: from theory to practice. Leading Edge 32, 1040–1054.

Pan, Y., Gao, L., 2020. Random objective waveform inversion of surface waves. Geophysics 85, EN49–EN61.

Pan, Y., Gao, L., Bohlen, T., 2019. High-resolution characterization of near-surface structures by surface-wave inversions: From dispersion curve to full waveform. Surveys in Geophysics 40, 167–195.

Pan, Y., Gao, L., Bohlen, T., 2021. Random-objective waveform inversion of 3d-9c shallow-seismic field data. Journal of Geophysical Research: Solid Earth 126, e2021JB022036. doi:https://doi.org/10.1029/2021JB022036.

Pan, Y., Xia, J., Xu, Y., Gao, L., Xu, Z., 2016. Love-wave waveform inversion for shallow shear-wave velocity using a conjugate gradient algorithm. Geophysics 81, R1–R14.

Pasquet, S., Bodet, L., Dhemaied, A., Mouhri, A., Vitale, Q., Rejiba, F., Flipo, N., Guérin, R., 2015. Detecting different water table levels in a shallow aquifer with combined p-, surface and sh-wave surveys: Insights from vp/vs or poisson's ratios. Journal of Applied Geophysics 113, 38–50.

Pasquet, S., Holbrook, W.S., Carr, B.J., Sims, K.W.W., 2016. Geophysical imaging of shallow degassing in a yellowstone hydrothermal system. Geophysical Research Letters 43, 12,027–12,035.

Romdhane, A., Grandjean, G., Brossier, R., Rejiba, F., Virieux, J., 2011. Shallow-structure characterization by 2d elastic full-waveform inversion. Geophysics 76, R81–R93.

Schäfer, M., Groos, L., Forbriger, T., Bohlen, T., 2014. Line-source simulation for shallow-seismic data. part 2: full-waveform inversion—a synthetic 2-d case study. Geophysical Journal International , 1405–1418.

Tillmann, A., Englert, A., Nyari, Z., Fejes, I., Vanderborght, J., Vereecken, H., 2008. Characterization of subsoil heterogeneity, estimation of grain size distribution and hydraulic conductivity at the Krauthausen test site using cone penetration test. Journal of contaminant hydrology 95, 57–75.

Tran, K.T., Mcvay, M., Faraone, M., Horhota, D., 2013. Sinkhole detection using 2d full seismic waveform tomography. Geophysics 78, R175–R183.

Tronicke, J., Holliger, K., Barrash, W., Knoll, M.D., 2004. Multivariate analysis of cross-hole georadar velocity and attenuation tomograms for aquifer zonation. Water Resources Research 40, W01519.

Uyanik, O., 2011. The porosity of saturated shallow sediments from seismic compressional and shear wave velocities. Journal of Applied Geophysics 73, 16–24.

Vereecken, H., Döring, U., Hardelauf, H., Jaekel, U., Hashagen, U., Neuendorf, O., Schwarze, H., Seidemann, R., 2000. Analysis of solute transport in a heterogeneous aquifer: the Krauthausen field experiment. Journal of Contaminant Hydrology 45, 329–358.

Virieux, J., Operto, S., 2009. An overview of full-waveform inversion in exploration geophysics. Geophysics 74, WCC1–WCC26.

Xia, J., Miller, R.D., Park, C.B., 1999. Estimation of near-surface shear-wave velocity by inversion of rayleigh waves. Geophysics 64, 691–700.

Xing, Z., Mazzotti, A., 2019. Two-grid full-waveform rayleigh-wave inversion via a genetic algorithm: part 1 - method and synthetic examples. Geophysics , 1–66.

Yang, P., Brossier, R., Métivier, L., Virieux, J., Zhou, W., 2018. A time-domain preconditioned truncated newton approach to visco-acoustic multiparameter full waveform inversion. SIAM Journal on Scientific Computing 40, B1101–B1130.

Yu, Y., Huisman, J.A., Klotzsche, A., Vereecken, H., Weihermüller, L., 2022. Coupled full-waveform inversion of horizontal borehole ground penetrating radar data to estimate soil hydraulic parameters: A synthetic study. Journal of Hydrology 610, 127817. doi:https://doi.org/10.1016/j.jhydrol.2022.127817.

Yu, Y., Weihermüller, L., Klotzsche, A., Lärma, L., Vereecken, H., Huisman, J.A., 2021. Sequential and coupled inversion of horizontal borehole ground penetrating radar data to estimate soil hydraulic properties at the field scale. Journal of Hydrology 596, 126010. doi:https://doi.org/10.1016/j.jhydrol.2021.126010.